Simulations of Neutrons in Extensive Air Showers

Martin Schimassek,[a,b,*] **Ralph Engel,**[b,c] **Alfredo Ferrari,**[b] **Markus Roth,**[b] **David Schmidt**[c] **and Darko Veberič**[b]

[a] *CNRS/IN2P3, IJCLab* **·UC**Lab*, Université Paris-Saclay, Orsay, France*

[b] *Karlsruhe Institute of Technology* **KIT**, *Institute for Astroparticle Physics, Germany*

[c] *Karlsruhe Institute of Technology* **KIT**, *Institute of Experimental Particle Physics, Germany*

E-mail: martin.schimassek@ijclab.in2p3.fr

The neutron cloud of an air shower differs significantly from its well-studied electromagnetic and muonic shower components. Neutrons are the only neutral hadrons that are stable on the time scales of air showers. Due to their neutrality, the energy losses of neutrons are minimal at low energies. Combined with their stability on the time scales of air showers, these make them highly abundant at the ground. However, they are difficult to detect and simulate due, in part, to the low energies involved. We present results based on the FLUKA simulation package, which accurately describes the propagation and production of neutrons from the highest energies down to thermal ones. By comparing the resulting energy spectra, arrival times, and lateral distributions with those of muons, we highlight the abundance of neutrons and their importance in air showers. Finally, we investigate the possibility of using neutrons as additional tracers of hadronic interactions in air showers and the implications of their measurement for testing hadronic interaction models.

*Speaker

1. Introduction

Neutrons are unique particles in air showers as the only electrically neutral massive particle stable on the relevant time scales. Already in early works, e.g. Ref. [1], these properties were used to infer that low energy particles with these properties would arrive significantly delayed. Linsely [2] observed such subliminal particles in air showers and could provide estimates of the total energy in the neutron component. More modern examples of dedicated neutrons measurements can be found in Refs. [3–5] and recent observations of late-arriving particles in air-showers in Ref. [6]. The caveat in the interpretation of such measurements is and has been the lack of detailed understanding of the neutron component expected from air showers. Building on previous work [7], we analyse a set of dedicated simulations including neutrons of all energies in this contribution. After introducing the simulation set-up in Section 2, we deepen the understanding of the expected neutron energy spectra in Section 3 and highlight numerical coincidences of the scaling with energy and primary mass in Section 4.

2. Simulation Method

To study the properties of neutrons in air showers we use FLUKA[1] [8, 9] in a setup similar to previous studies [7]. In contrast to dedicated codes for air shower simulations, FLUKA allows us to simulate neutrons from the highest energies down to thermal energies, making it an ideal tool for this study. The predictions of FLUKA for air shower simulations have been validated with measurements before, both for muon spectra [10, 11] and for nucleons spectra [12–14].

For our studies, showers of three different representative primaries – photons, protons, and iron nuclei – are simulated at vertical incidence with Earth's atmosphere described by 100 layers with densities following the US Standard Atmosphere. Hadrons and leptons are simulated with all relevant physics processes, unstable particles are allowed to decay, annihilate, or be captured, down to 5 MeV, with the exception of neutrons which are transported down to 10^{-5} eV. We simulate at five different primary energies from 5.6×10^{14} to 5.6×10^{18} eV and store energy spectra of muons, neutrons, and anti-neutrons at different observation depths. Relevant for the presented work are the depths of 675 g/cm^2 – roughly the atmospheric depth of IceTop [15] – and the ground level at 1033 g/cm^2. The atmosphere is assumed to be dry, and for the ground level at 1033 g/cm^2 a typical soil composition with some moisture is adopted, while for the layer at 675 g/cm^2 a separate simulation run with an ice layer as ground is used. We capture the radial and temporal features by storing the particle energy spectra separate for radial and time bins. The radial bins cover typical scales of showers at 10^{16} eV with five bins up to $R > 400$ m, while the time bins start at 10^{-1} ns for muons and 1 ns for neutrons and reach up to the millisecond scale in steps of $10^{-1/3}$ ns.

To resolve the longitudinal development of the showers, we additionally collect the accumulated physical track length ℓ of muons and neutrons in each of the 100 layers of the atmosphere. To convert the track length into a fluence f per shower for the atmosphere layer i, we use the density ρ_i and the thickness of the each layer ΔX_i as $f(X_i) = \rho_i \ell_i / \Delta X_i$. The resulting dimensionless quantity can be understood as follows: Multiplying the physical track length ℓ with the density yields a effective grammage crossed by all particles, and the normalisation to the thickness of the layer results in a
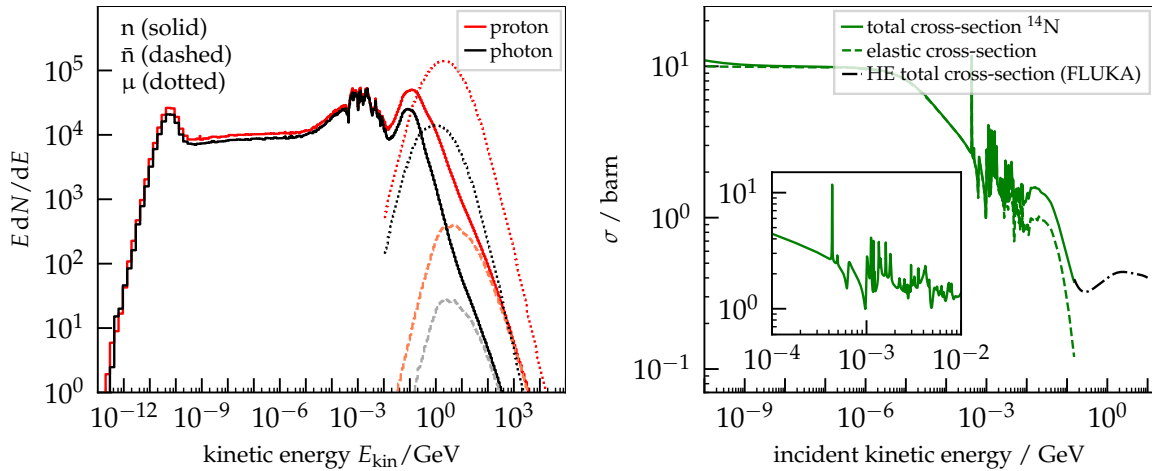
---

[1]www.fluka.org

2

Figure 1: *Left:* Energy spectra of neutrons (solid lines), anti-neutrons (dashed), and muons (dotted) for proton and photon showers at $E = 5.6{\times}10^{16}$ eV primary energy counted at ground level. *Right:* Total (solid) and elastic (dashed) cross-section of neutrons on nitrogen with data taken from ENDF/B-VIII.0 [16] below 150 MeV, and above from FLUKA with an inset highlighting the structures around 1 MeV.

unit-less fluence. Compared to defining the fluence with vertical slices crossed by particles in the longitudinal profile, this method results in values that better represent low-energy particles as the full angular distribution is included.

3. Understanding the Energy Spectra of Neutrons

As first step to understand the neutron component of air-showers, we want to describe the energy spectrum of neutrons. The energy spectrum contains information about the main production mechanisms and propagation processes relevant to neutrons in air showers. The left panel of Fig. 1 shows the energy spectrum of neutrons of showers of $E = 5.6{\times}10^{16}$ eV at ground level at $X_{\text{det}} = 1033$ g/cm^2. It spans 15 orders of magnitude in neutron energy from the thermal peak[2] at about 10^{-11} GeV up to a high energy tail of 10^3 GeV. For comparison, muons are shown as dotted lines in the same panel. Because muons are unstable on the scale of the shower development, their abundance below a few hundred MeV is suppressed. Similarly, we see the same suppression for the anti-neutrons shown with dashed lines in the same figure albeit because of annihilation not decay.

The comparison of neutron and anti-neutron spectra also reveals that, at the highest energies, neutrons are "pair-created" in hadronic interactions while at lower energies, photo-nuclear interactions are more important. To highlight the importance of the photo-nuclear interactions, we can compare the neutron spectrum of protons and photon primaries in the range of a few MeV. The similarity – that does not exist on this level at the highest energies – clearly indicates the photo-nuclear origin of these neutrons. The approximate flat spectrum in the range of 10^{-9} to 10^{-5} GeV is a result of an almost diffusive propagation regime. In this energy range, the cross-section $\sigma(E)$ – shown in the right panel of Fig. 1 – is dominated by elastic interactions and approximately energy-independent. From classical mechanics, the minimal energy after an elastic collision can be written

---

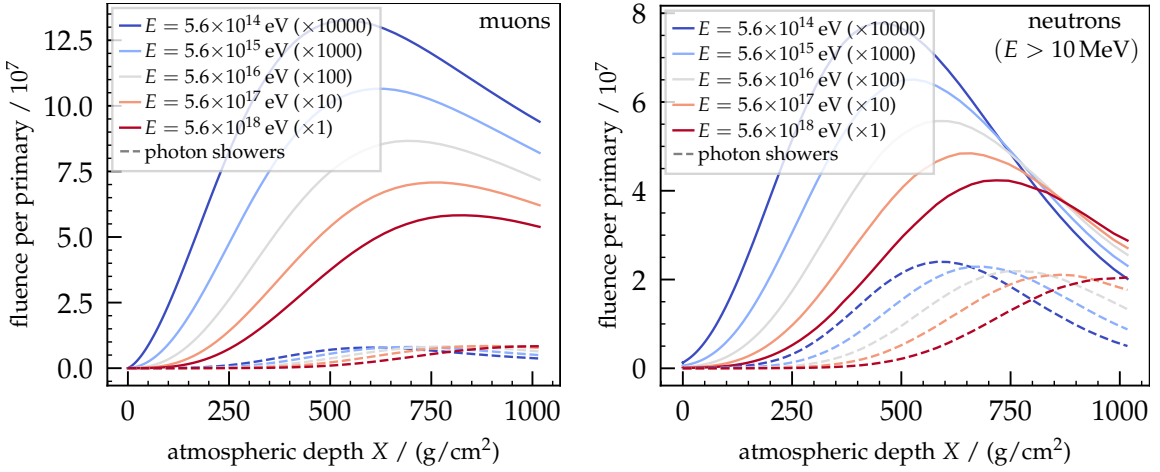[2]At a temperature of 20°C we expect $E \approx k_{\text{B}}T = 25$ meV.

3

Figure 2: Comparison of the energy scaling of particles in simulation. The particle fluences are scaled with E^{-1} to highlight deviations from linear scaling. *Left:* Fluences of muons in iron (solid) and photon (dashed) showers. *Right:* Fluence of neutrons with kinetic energies greater than $10\,\text{MeV}$ for iron and photon showers.

as $E'_{\text{min}} = \alpha E$ with α depending on the particle masses. Due to isotropy in the center of mass frame, the probability distribution of the energy E' of the neutron after scattering, $P(E{\to}E')$, is uniform between E'_{min} and $E' = E$. The propagation of the neutrons through the atmosphere leads to the development of a low-energy tail in the neutron distribution. This tail grows until a neutron energy distribution close to $\Phi(E) = C/E$ is reached, for which the energy spectrum of down-scattered neutrons (after a further step of interactions) is again a $1/E'$ distribution

$$\Phi(E') \sim \int_{E'}^{\frac{E'}{\alpha}} P(E{\to}E')\,\sigma(E)\,\Phi(E)\,\mathrm{d}E. \qquad (1)$$

The $1/E$ spectrum of neutrons is a good approximation in this energy range over a wide range of atmospheric depths.

At higher energies of a few MeV, this discussion breaks down due to the resonance peaks, clearly visible in the inset in Fig. 1 (right). The structure of the cross-section is clearly visible also in the energy spectrum. Around a few hundred MeV, the minimum in the cross-section visible in the right panel of Fig. 1 leads to the so-called quasi-elastic peak in the neutron spectrum.

4. Understanding the Scalings

Following the discussion of the energy spectrum of neutrons itself, we aim to determine how the spectra scale with different primary mass and primary energy. As shown in previous work [7, 18], the scalings are not following the simple expectation but rather result in two numerical coincidences. We highlight these coincidences by using the longitudinal profiles derived from the fluence introduced in Section 2 to show the scaling behaviour. Fig. 2 shows the longitudinal profiles of muons (left) and neutrons (right) for iron and photon showers of different energies. To achieve visual congruence in case of linear scaling with energy, we scale the profiles with $5.6{\times}10^{18}\,\text{eV}/E$. For muons, in the left panel of Fig. 2 we see a scaling of E^{β} with $\beta < 1$ as expected from the Heitler-Matthews model [19], both at the ground and at the respective maxima. Contrary, for neutrons in the right
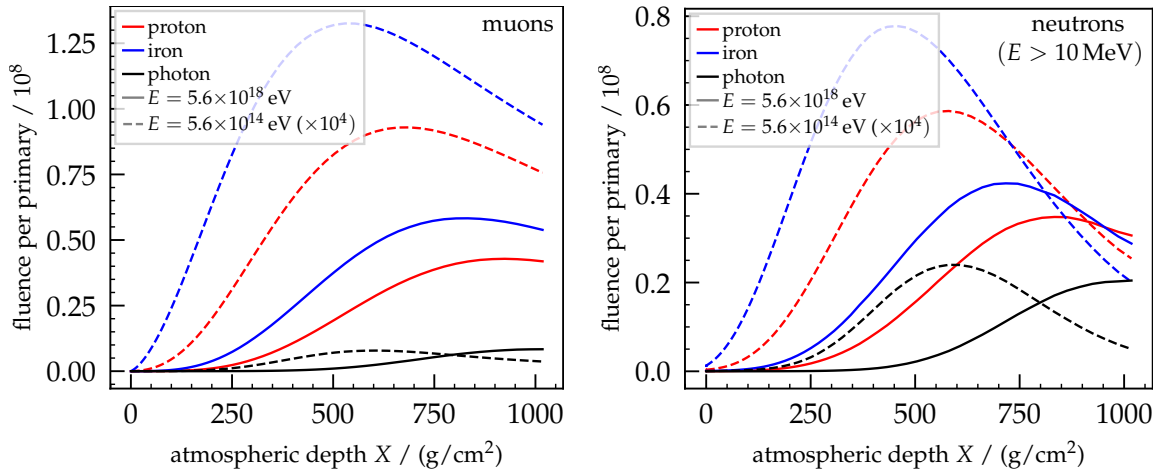
Figure 3: Comparison of the fluence of particles for photon showers (black), proton showers (red), and iron showers (blue) at two energies multiplied to cancel linear scaling. Muon fluence in the *left* panel, neutrons with kinetic energies above 10 MeV on the *right*.

panel, we only see this scaling in the maxima of the profiles. For ground level, we can observe even $\beta > 1$, while for a large range of typical observation depths (~800 to 900 g/cm^2) almost linear scaling is seen. From the shape of the profiles, it is clear that this quasi-linear behaviour is due to the larger attenuation of the neutrons in air combined with the shift of the shower maximum. At ground level and the energy range investigated here, the two effects cancel creating the surprisingly linear scaling with energy. This result is not strongly dependent on the chosen threshold kinetic energy of 10 MeV shown in Fig. 2 but rather valid for a broad range of neutron energies from MeV to 100 GeV [7].

In the case of photon showers, the approximate linear scaling with energy at the maximum is clearly visible for neutrons and also for muons, albeit the relative abundance with respect to hadronic showers is clearly different for muons and neutrons. To further understand the differences in neutron numbers between primaries, we compare directly the longitudinal fluence profiles of proton, iron, and photon showers for two energies scaled the same way as before in Fig. 3. For muons in the left panel, we can observe the expected difference between the two hadronic primaries in the maximum of the profiles but also at ground level, as the different attenuation factors from maximum to the ground only reduce the difference. In the right panel, for neutrons above 10 MeV kinetic energy, the situation is different and resembles the coincidence seen in the energy evolution. While the maximal number of neutrons produced follows the expected hadronic shower scaling, with about 30% more neutrons for iron than for proton primaries, at ground level proton and iron showers have almost identical neutron fluences. This observation holds for all energies considered in this study at vertical incidence, as is visible from the behaviour of the two extreme energies shown in Fig. 3. The mechanism is similar to the coincidence in energy scaling: lighter primaries have – on average – deeper shower maxima which in turn reduce the attenuation of neutrons to ground level. Coincidentally, these two effects cancel also here, and similarly to the energy scaling, this effect is independent of the neutron energy threshold above a few MeV and below the highest energies of several hundred GeV. Another interesting observation is that the relative abundance of neutrons
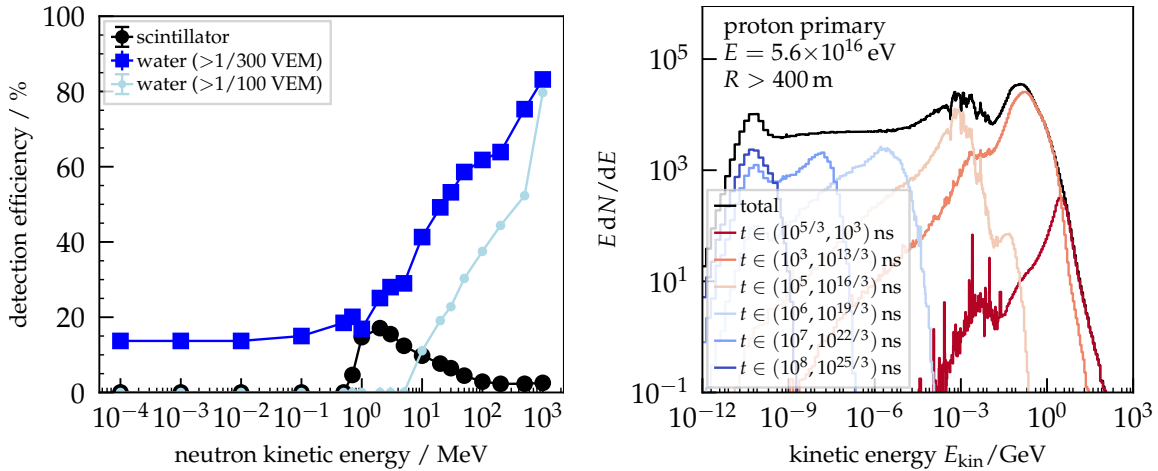
Figure 4: *Left:* Approximate neutron detection efficiency in simplified simulations of detectors of different types and thresholds. *Right:* Energy spectrum of neutrons from $E = 5.6 \times 10^{16}$ eV proton primary and more than 400 m from the shower axis at the ground, highlighting the different delays from early (red) to late (blue).

in photon showers is larger than in the muon component. In this case, the expected differences of photon showers from hadronic ones in neutron fluence at ground does depend on the energy, as visible from the relative increase of the black dashed to solid lines in the right panel of Fig. 3.

5. Prospects of Detection

To gauge the possibility of detecting the neutron component of air-showers in current experiments, we want give indicative detection probabilities for typical detector types as well as investigating the time and radial distributions that can be used to identify phase space sections with larger probability of significant influence of the neutron component on the overall particle content. Starting from semi-isotropic, mono-energetic neutrons, a 1 cm thick infinite scintillator and 120 cm high water layer – similar to the surface detector of the Pierre Auger Observatory [20] – are simulated and all signals above given thresholds are recorded to estimate the detection efficiency. For the scintillator, a threshold of 100 keV electron equivalent (~6% of a minimum ionizing particle signal) is used. For the water-Cherenkov set-up, we use two thresholds expressed as fraction of the most probable signal of a vertical muon (VEM): 1/100 VEM and 1/300 VEM. The results of these calculations are shown in the left panel of Fig. 4. From the comparison of the two thresholds for water, we can see that, at low neutron energies, only photons from nuclear interactions are able to produce Cherenkov light. These photons can only produce small (localized) signals that can be difficult to detect experimentally. The importance of the thickness of the detector can be seen by comparing the detection efficiency difference between the water and scintillator set-up at high energies. Overall, we can derive from this simulation that neutrons at and above 1 MeV are likely detectable, while the exact thresholds will depend critically on the exact experimental set-up including quenching factors, and surrounding materials creating back-reflections of neutrons.

With the knowledge of the likely energy range accessible in detectors, we can assess the typical time delays of such neutrons. We use the logarithmically time binned data introduced in Section 2 and show a subset of the time bins for neutrons in the right panel of Fig. 4, focusing on neutrons
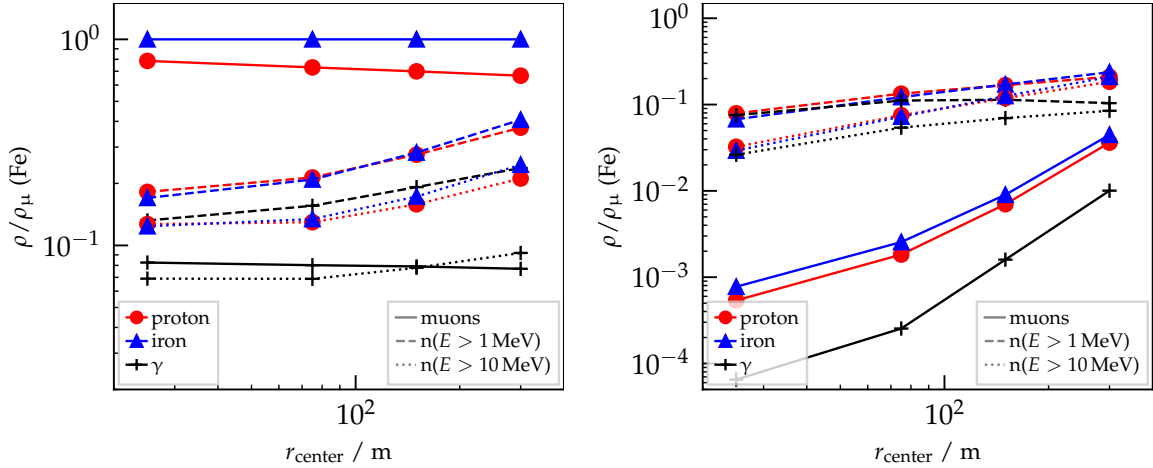
Figure 5: Comparison of the radial distributions of muons and neutrons for different primaries at $E = 5.6 \times 10^{16}$ eV and measured at $X_{\text{det}} = 675$ g/cm^2. The densities are computed inside radial bins and shown at the arithmetic center of each bin, relative to the total muon density of iron showers. *Left:* Total time integrated particle content without the simulated ground. *Right:* With additionally a ground layer of ice and a time cut $t \in [1, 21.5)$ μs in arrival delay is applied.

far from the shower core ($R > 400$ m) at ground level. We can see that, for typical time scales of up to 1 μs, only the highest neutron energies contribute that are not very abundant. For delays of the order of several μs, a sizeable fraction of the MeV neutrons and most of the quasi-elastic peak is included. The lower energies down to the thermal peak arrive at times clearly beyond the reach of typical cosmic-ray experiments at the scale of milliseconds.

To compare the abundances of neutrons and muons quantitatively, we use the binned lateral particle densities relative to the muon density of iron showers shown in Fig. 5. We use two different neutron kinetic energy thresholds, 1 and 10 MeV, to highlight the importance of energy threshold and the applicable timing constraints. If only the energy thresholds are considered and all arrival times are integrated, we obtain the relative densities of the left panel. Neutrons above 1 MeV reach up to 40% of the density of muons with the previously discussed minuscule difference between proton and iron at 400 m. At the higher 10 MeV threshold this ratio drops by about 10%. If, in order to capture the typical time scales of experiments, we restrict the arrival times to a window of $[1, 21.5)$ μs, the interpretation changes as evident from the right panel of Fig. 5. The muon density drops significantly, with respect to the same reference density, as the majority of muons arrives earlier. For the neutrons the important feature is that observable densities within this time cut, at large core distances, depend only slightly on the applied energy threshold: the dashed and dotted lines corresponding to the two thresholds align within a few percent. The differences between hadronic primaries are small and might not be resolvable experimentally. For photon showers, differences of about a factor two with respect to hadronic primaries at large distances seem interesting for the discrimination of photon primaries. However, a key ingredient for a full prediction of the actual detectability is the signal per particle that is not accounted for in Fig. 5. As these signals, just like the detection efficiency, might depend critically on experimental details, we leave these calculations for future work.

6. Conclusions

In this work, we show that the neutron component, due solely to its abundance in air-showers, deserves detailed study. Because of the very different characteristics of neutrons in energy spectrum, arrival times, and interaction in the detector, detailed predictions are difficult. Our results highlight, that, while the typical signals from neutrons are likely small in typical regions of arrival time and radius, the detection efficiency can be of the order of 10 to 50% for fairly abundant MeV-neutrons and are thus clearly not negligible. It is important to stress that there are large dependencies of the detection efficiency and signal sizes on the signal threshold, quenching, and other experimental parameters. Thus, the numbers derived here should be taken as purely indicative and for any quantitative prediction for a given experiment additional detailed simulations are necessary. In general, we find that the neutrons trace the hadronic component of the shower but, due to numerical coincidences of compensating $X_{\max}$ shift with attenuation, show little prospect for primary identification at vertical incidence. This statement is strictly true only for a given ground level and range of primary energy, as the "cross-over" point of proton and iron in neutron fluence shift to greater depths with rising energies, from about $700\,\text{g/cm}^2$ at $5.6\times10^{14}\,\text{eV}$ to $950\,\text{g/cm}^2$ at $5.6\times10^{18}\,\text{eV}$. Hence, at even higher energies more neutrons at the ground from heavier primaries are expected. How significant these differences can be in real experiments remains to be determined by future detailed studies.

References

[1] V.C. Tongiorgi, Phys. Rev. **75** (1949) 1532–1540, doi: 10.1103/PhysRev.75.1532.

[2] J. Linsley, J. Phys. G **10** (1984) L191–L195, doi: 10.1088/0305-4616/10/8/005.

[3] A. Shepetov *et al.*, Eur. Phys. J. Plus **135** (2020) , doi: 10.1140/epjp/s13360-019-00092-1.

[4] Y.V. Stenkin *et al.*, Phys. Atom. Nucl. **70** (2007) 1088–1099, doi: 10.1134/S1063778807060117.

[5] A.D. Erlykin, Nucl. Phys. B Proc. Suppl. **175-176** (2008) 330–333, doi: 10.1016/j.nuclphysbps.2007.11.024.

[6] P. Abreu *et al.* [Pierre Auger], **PoS** (ICRC2021) 218, doi: 10.22323/1.395.0218.

[7] R. Engel *et al.*, **PoS** (ICRC2021) 492, doi: 10.22323/1.395.0492.

[8] A. Ferrari *et al.*, CERN-2005-010, SLAC-R-773, INFN-TC-05-11, (2005), doi: 10.5170/CERN-2005-010.

[9] T.T. Böhlen *et al.*, Nucl. Data Sheets **120** (2014) 211–214, doi: 10.1016/j.nds.2014.07.049.

[10] G. Battistoni *et al.*, Astropart. Phys. **17** (2002) 477–488, doi: 10.1016/S0927-6505(01)00176-1.

[11] G. Battistoni *et al.*, Nucl. Phys. B Proc. Suppl. **168** (2007) 286–288, doi: 10.1016/j.nuclphysbps.2007.02.025.

[12] P. Zuccon *et al.*, Astropart. Phys. **20** (2003) 221–234, doi: 10.1016/S0927-6505(03)00160-9.

[13] A. Ferrari *et al.*, Radiat. Prot. Dosim. **93(2)** (2001) 101, doi: 10.1093/oxfordjournals.rpd.a006418.

[14] N. Combier *et al.*, IEEE Trans. Nucl. Sci. **64** (2017) 614–621, doi: 10.1109/TNS.2016.2611019.

[15] R. Abbasi *et al.* [IceCube], Nucl. Instrum. Meth. A **700** (2013) 188-220, doi: 10.1016/j.nima.2012.10.067.

[16] D.A. Brown *et al.*, Nucl. Data Sheets **148** (2018) 1–142, doi: 10.1016/j.nds.2018.02.001.

[17] E.E. Lewis, *Fundamentals of Nuclear Reactor Physics*, (Elsevier 2008), ISBN 978-0-080-56043-4.

[18] R. Engel *et al.*, EPJ Web Conf. **283** (2023) 05006, doi: 10.1051/epjconf/202328305006.

[19] J. Matthews, Astropart. Phys. **22** (2005) 387–397, doi: 10.1016/j.astropartphys.2004.09.003.

[20] A. Aab *et al.* [Pierre Auger], Nucl. Instrum. Meth. A **798** (2015) 172–213, arXiv: 1502.01323.